Active Damping: An $\mathcal{H}_\infty$ Model Reference Approach

Jorge Pérez, *Member, IEEE*, Santiago Cóbreces, *Member, IEEE*, Robert Griñó, *Senior Member, IEEE*, Francisco Huerta, *Member, IEEE*, and Francisco J. Rodríguez Sánchez, *Member, IEEE*

***Abstract*—This paper focuses on the design of an active-damping controller that shapes the dynamics of an *LCL* grid connected voltage source converter (VSC) to mimic an *L*-filter connected VSC. This makes possible to use simpler classical proportional plus resonant or proportional plus integral controllers design methods to regulate the grid current with minimum penalties in both performance and stability margins. The active-damping design follows a model-reference approach and is synthesized through a (sub)optimal $\mathcal{H}_\infty$ algorithm. The controller uses the grid current and point of common coupling voltage, although it allows the selection of a different set of measurements. Effectiveness of the method is demonstrated with time- and frequency-domain experimental results.**

***Index Terms*—Power converter, current control, H-infiinty control, robustness.**

I. Introduction

DISTRIBUTED power generation systems generally rely on the use of controlled pulse-width-modulation (PWM) converters as their grid-connection interfaces for energy conversion and conditioning. Multiple objectives can be achieved by implementing a suitable current controller, such as adjustable power factor, controllable dc-link voltage, or reduced line current harmonic distortion [1]. To ensure low total harmonic distortion (THD) grid currents, a filter that reduces PWM commutation ripple is connected between the voltage source converter (VSC) and the grid. One of the most common is the *LCL* filter, due to its good cost-filtering capabilities ratio [2].

In opposition to the simpler *L*-filter, the use of an *LCL* filter increases control complexity as it introduces a pair of complex-conjugated poles close to the $j\omega$ axis that may cause current oscillations in response to system disturbances, which may lead to system instability in the presence of ill-conditioned closed-loop systems [3] or weak grids [2].

The progressive advance of *LCL* use has motivated two alternative control approaches. The first group is formed by standard single-loop approaches, usually more sophisticated than those used for *L*-design, which directly consider *LCL* dynamic complexity in the design process [4]–[7]. A second group proposes the use of several strategies to damp *LCL* resonances, which, once applied, present to the reference-tracking controller, a simplified dynamic model keeping its design simple. This category is divided into passive—hardware—or active—software—approaches. The proposal on this paper belongs to the latter category.

Passive damping [8]–[12] adds passive elements, commonly resistances, to the filter. This simple solution comes at the cost of extra power losses and, in some cases, reduction of the high-frequency attenuation capability [10].

Active-damping techniques [1], [2], [13]–[19] try to achieve similar objectives dividing the design into two stages: A first stage that damps resonances, usually using an extra inner control loop, and a second stage consisting in the design of a reference-tracking controller that faces a simplified plant, ideally one similar to an *L*-filter dynamic model. This lossless simplification of the outer controller makes active damping very popular on both industry and academia.

Most active-damping methods are based on the emulation of a virtual resistance in some position of the grid filter. Approaches usually operate using the measurement of at least one extra *LCL*-filter state, commonly the capacitor voltage (or current), in addition to the controlled (grid side or converter side) current [15], [17], [19]. Other proposals include more filter measurements to achieve better results [20].

A second group of active-damping methods try to achieve the same objective using the already available current measurement, without increasing the number of sensors. They are sometimes referred as filter-based active damping. Two main options exist in this category: The use of a lead-lag network (high-pass filter) [15], [21], to avoid negative gain margins placing extra gain on problematic frequencies, and the use of a notch filter, to attenuate the resonance by means of adjusting the antiresonance peak of the notch filter at the resonance frequency of the *LCL* filter [22], [23].

This paper proposes an active-damping approach that consists in the introduction of an inner control loop that makes the resulting plant emulates the dynamic behavior of an *L*-filter connected converter. This inner controller is designed using a

Manuscript received March 18, 2017; revised July 16, 2017 and September 13, 2017; accepted September 20, 2017. Date of publication October 12, 2017; date of current version April 20, 2018. The work of S. Cóbreces and F. J. Rodríguez Sánchez was supported in part by the Ministerio de Economía, Industria y Competitividad and Agencia Estatal de Investigación under Projects DPI2017-88505-C2-2-R and ENE2014-57760-C2-2-R, and in part by Universidad de Alcalá under Project CCG2015/EXP-064. The work of R. Grino was supported in part by the Government of Spain through the Ministerio de Economía, Industria y Competitividad, and Agencia Estatal de Investigación under Projects DPI2013-41224-P and DPI2017-85404-P. Recommended for publication by Associate Editor L. Zhang. *(Corresponding author: Santiago Cóbreces.)*

J. Pérez is with Gamesa Electric S.A.U., Madrid 28823, Spain (e-mail: jorge.perez@depeca.uah.es).

S. Cóbreces and F. J. Rodríguez Sánchez are with the Department of Electronics, Universidad de Alcalá, Alcalá de Henares 28871, Spain (e-mail: cobreces@depeca.uah.es; franciscoj.rodriguez@uah.es).

R. Griñó is with the Institute of Industrial and Control Engineering, Universitat Politècnica de Catalunya, Barcelona 08028, Spain (e-mail: roberto.grino@upc.edu).

F. Huerta is with Carlos III University of Madrid, Madrid 28911, Spain (e-mail: fhuerta@ing.uc3m.es).

Color versions of one or more of the figures in this paper are available online at http://ieeexplore.ieee.org.

Digital Object Identifier 10.1109/TPEL.2017.2762469

See http://www.ieee.org/publications_standards/publications/rights/index.html for more information.

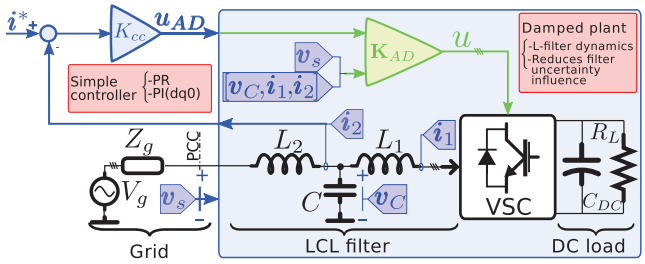

Fig. 1. Block-diagram description of the proposed active-damping approach.

model-reference optimal $\mathcal{H}_\infty$ approach that translates this design complexity into a convex optimization problem, with guaranteed performance. The high accuracy of the emulation allows directly using the controller that would be used in the *L*-filter case with almost identical results.

The proposal avoids the virtual-resistor paradigm, which was actually problematic in the most typical digital control scenario [21], [24], [25] and directly faces one of the active-damping deeper objectives to make the *LCL* filter as easy to control as the *L*-filter, obtaining its improved filtering and cost advantages without worrying about its dynamic particularities—resonances.

The casting of the problem inside the $\mathcal{H}_\infty$ problem converts the design process in an almost systematic procedure that formally guarantees an optimal controller calculated only from converter parameters, making it suitable for its implementation in a software tool that may be of interest for its industrial use. This easy design flow contrasts with that of traditional active-damping approaches, which usually involve nontrivial design iterations, with nonconvex optimization algorithms, parameter sweeping, and outer controller retuning that may not success. $\mathcal{H}_\infty$ control is not new in grid converters control [26]–[32] but has not been explored for the active-damping topic.

One inherent advantage of this proposal with respect to previous approaches is its flexibility regarding the measurements needed, offering very accurate results measuring only one or several of the filter variables: converter current, grid current, and/or capacitor voltage. When compared with previous approaches that only use one current measurement, perhaps the most interesting configuration, it offers better performance in the achieved damping and also in the resulting plant phase, which keeps positive on wide frequency regions. This fact is known to have important stability and robustness implications [33].

Next section develops open- and closed-loop dynamics of the proposed application. Section III is centered on the proposed controller, its design, synthesis, implementation, and limitations. Experimental results of the proposed method, both in time and frequency domains, are shown in Section IV, as well as the analysis of the robustness of stability and damping and its performance comparison with related classical-damping approaches. Finally, the paper conclusions can be found in Section V.

II. Problem Description and Modeling

Fig. 1 shows a simplified scheme of the considered application: A current-control loop of a VSC connected to the grid through an *LCL* filter.

Instead of facing this objective directly, in a single loop, this paper proposes to use nested control loops. In the inner loop of the control scheme shown in Fig. 1, the damping controller $\boldsymbol{K}_{AD}$ will reshape the *LCL*-filter open-loop dynamics so it resembles one of the simpler *L*-filters. Then, a simple outer grid-current controller (K_{cc} in Fig. 1), such as classic proportional plus resonant (PR) and proportional plus integral (PI) regulators, can be designed for this emulated *L*-filter dynamic.

The design methodology is intended for three-phase system. The problem is approached in uncoupled $\alpha\beta$ axes [34], reducing the original three-phase problem to two identical single-phase problems. For notation simplicity, only one of the controlled channels is considered in this paper for both plant modeling and controller design.

A. Open-Loop Modeling

System information can be obtained from three measurable variables (states): The grid- and converter-side currents i_2 and i_1, and the capacitor voltage v_c. Although the presented methodology is able to operate only with i_2, which is perhaps the most interesting case, the method is also able to work with a different set of measured variables.

Those variables are affected by two inputs: The VSC average output voltage over a PWM period u (the control variable) and the measured point of common coupling (PCC) voltage v_s (the disturbance variable), as it is shown in the following equation:

$$\underbrace{\begin{bmatrix} I_2 \\ I_1 \\ V_c \end{bmatrix}}_{\boldsymbol{X}(s)} = \underbrace{\begin{bmatrix} F_{u\to i_2} \\ F_{u\to i_1} \\ F_{u\to v_c} \end{bmatrix}}_{\mathbf{G}(s)} U(s) + \underbrace{\begin{bmatrix} F_{v_s\to i_2} \\ F_{v_s\to i_1} \\ F_{v_s\to v_c} \end{bmatrix}}_{\mathbf{G}_d(s)} V_s(s) \tag{1}$$

where $\mathbf{G}(s)$ and $\mathbf{G}_d(s)$ are the multiple-input multiple-output (MIMO) dynamics from $U(s)$ and $V_s(s)$, respectively, to the measurements vector $\boldsymbol{X}(s)$, represented in the Laplace domain. These matrices are broken down as follows:

$$F_{u\to i_2}(s) = -\frac{Y_{L_2}\cdot Z_C\cdot Y_{L_1}}{1+Z_C\cdot(Y_{L_1}+Y_{L_2})} \tag{2}$$

$$F_{v_s\to i_2}(s) = \frac{Y_{L_2}\cdot(1+Y_{L_1}\cdot Z_C)}{1+Z_C\cdot(Y_{L_1}+Y_{L_2})} \tag{3}$$

$$F_{u\to i_1}(s) = -\frac{Y_{L_1}\cdot(1+Y_{L_2}\cdot Z_C)}{1+Z_C\cdot(Y_{L_1}+Y_{L_2})} \tag{4}$$

$$F_{v_s\to i_1}(s) = \frac{Y_{L_2}\cdot Z_C\cdot Y_{L_1}}{1+Z_C\cdot(Y_{L_1}+Y_{L_2})} \tag{5}$$

$$F_{u\to v_c}(s) = \frac{Y_{L_1}\cdot Z_C}{1+Z_C\cdot(Y_{L_1}+Y_{L_2})} \tag{6}$$

$$F_{v_s\to v_c}(s) = \frac{Y_{L_2}\cdot Z_C}{1+Z_C\cdot(Y_{L_1}+Y_{L_2})} \tag{7}$$

with

$$Y_{L_2}(s)=\frac{1}{L_2 s+R_2},\quad Y_{L_1}(s)=\frac{1}{L_1 s+R_1},\quad Z_C(s)=\frac{1}{C\cdot s}$$

where L_1, L_2 are the *LCL* converter and grid-side inductances, R_1, R_2 are their equivalent losses resistances, and C is the *LCL*-filter capacitor.

B. Inner Closed-Loop Damped Grid-Current Dynamic

Active-damping controller $\mathbf{K}_{\text{AD}}$ calculates the VSC average ac voltage u from the selected filter measurements, the PCC voltage v_s, and the output of the outer grid-current controller u_{AD}

$$U = K_{v_s} V_s + K_u U_{\text{AD}} + K_{i_2} I_2 + K_{v_c} V_c + K_{i_1} I_1. \tag{8}$$

The philosophy underlying this procedure is the creation of a control structure that involves the original plant, hiding its dynamics, and presents to the outer controller a simplified model. The new plant actuation variable is U_{AD}.

Substituting (8) in (1), grid-current (i_2) dynamic can be derived

$$I_2(s) = G_{\text{AD}}(s) \cdot U_{\text{AD}}(s) + G_{d_{\text{AD}}}(s) \cdot V_s(s) \tag{9}$$

where $G_{\text{AD}}(s)$ and $G_{d_{\text{AD}}}(s)$ expressions are shown in (10) at the bottom of this page.

From the outer current controller K_{cc} perspective, G_{AD} and $G_{d_{\text{AD}}}$ represent the dynamic model of a new grid-current plant with two inputs: u_{AD}, which is controlled by K_{cc}, and the PCC voltage v_s, which is an external uncontrolled disturbance.

III. Active-Damping Design

This section is centered in the design of the controller $\mathbf{K}_{\text{AD}}$, its synthesis fundamentals, procedure, and limitations. The philosophy lying under this procedure is the seek for a controller that minimizes the difference between the response of the controlled plant, an *LCL*-filter grid-connected VSC, and that of the reference model, an *L*-filter grid-connected VSC. This minimization is faced from a $||\cdot||_\infty$ optimization point of view.

A. Methodology

The controller $\mathbf{K}_{\text{AD}}$ is computed by means of an $\mathcal{H}_\infty$ synthesis. The input information that is needed to start the synthesis process is integrated in the generalized plant $\mathbf{P}$ [35]. $\mathbf{P}$ is a virtual plant that contains information of the open-loop system dynamics, the controller structure, and its performance objectives and constraints. Structurally, $\mathbf{P}$ is defined as follows:

$$\begin{bmatrix} \boldsymbol{z} \\ \boldsymbol{v} \end{bmatrix} = \mathbf{P} \begin{bmatrix} \boldsymbol{w} \\ \boldsymbol{u} \end{bmatrix} \tag{11}$$

where $\boldsymbol{w}$ is the exogenous inputs vector to the system (usually formed by closed-loop disturbances and references), $\boldsymbol{z}$ is the vector to be minimized by the synthesized controller (or errors vector), $\boldsymbol{u}$ is the actuation vector (outputs of the obtained controller to be applied to the plant input), and $\boldsymbol{v}$ is the measurements plant output (input to the obtained controller).

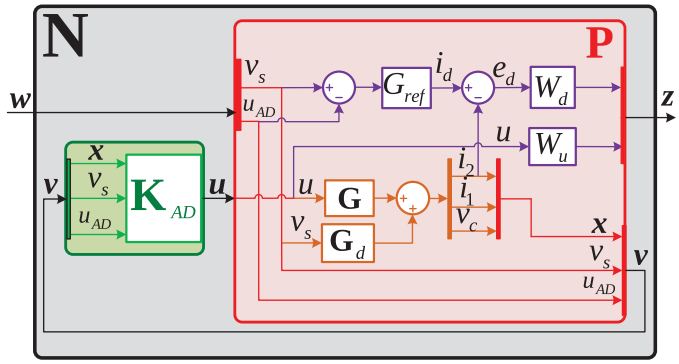

Fig. 2. Proposed generalized plant $\mathbf{P}$ is represented in red. Wrapped inside, the open-loop *LCL* plant (in orange) and a set of elements (in purple) added in the design process for controller synthesis. The desired active damping $\mathbf{K}_{\text{AD}}$ is shown in green. Connection of $\mathbf{P}$ and $\mathbf{K}_{\text{AD}}$ results in the virtual closed-loop system $\mathbf{N}$, in black.

With the information contained in $\mathbf{P}$, the synthesis algorithm will compute a (sub)optimal controller $\mathbf{K}_{\text{AD}}$, which minimizes the infinity norm[1] of the virtual closed-loop system $\mathbf{N}$ that results from the feedback interconnection of $\mathbf{P}$ and $\mathbf{K}_{\text{AD}}$, and relates exogenous input vector $\boldsymbol{w}$ and error vector $\boldsymbol{z} = \mathbf{N}\boldsymbol{w}$

$$\min_{\mathbf{K}_d} \left(\|\mathbf{N}(\mathbf{P}, \mathbf{K})\|_\infty = \max_{\boldsymbol{w}(\omega) \neq 0} \frac{\|\boldsymbol{z}(\omega)\|_2}{\|\boldsymbol{w}(\omega)\|_2} \right) \leq \gamma. \tag{12}$$

Thus, $\mathbf{K}_{\text{AD}}$ minimizes the energy of the error signals $\boldsymbol{z}$ for the *worst case direction* and *worst case frequency* of the input vector $\boldsymbol{w}$. The design keystone of this control paradigm is, then, to translate controller objectives to a proper definition of the generalized plant $\mathbf{P}$.

Fig. 2 shows the proposed structure for $\mathbf{P}$ (displayed in red color). The original *LCL* plant, $\mathbf{G}(s)$ and $\mathbf{G}_d(s)$—described in (1)—is displayed in orange. The extra elements added to incorporate design objectives into the problem are drawn in purple. Those elements generate an error signal e_d that compares the output current i_d of a reference model G_{ref} with that of the actual plant i_2.

A controller yielding a small e_d will make the closed-loop system mimic the dynamic behavior of the reference model, so e_d is included in the vector to minimize $\boldsymbol{z}$. Control signal u also needs to be included in $\boldsymbol{z}$ to avoid falling in a solution (i.e., controller) that needs an unrealistic control level and also to limit the effective control bandwidth. Transfer functions W_d and W_u are weighting functions that determine the range of frequencies where the reference model will be imitated (i.e.,

[1]The infinity norm of a MIMO system $\mathbf{H}(s)$ in the frequency domain is defined as $\|\mathbf{H}(s)\|_\infty \triangleq \sup_\omega \bar{\sigma}(\mathbf{H}(j\omega))$, where $\bar{\sigma}(\mathbf{H}(j\omega))$ is the maximum singular value of $\mathbf{H}(j\omega)$. For SISO systems that is simplified to $\|H(s)\|_\infty \triangleq \sup_\omega |H(j\omega)|$.

$$G_{\text{AD}}(s) = -\frac{K_u \cdot Y_{L_2} \cdot Z_C \cdot Y_{L_1}}{1 + Z_C \cdot (Y_{L_1} + Y_{L_2}) + (K_{i_1} \cdot (1 + Z_C \cdot Y_{L_2}) + (K_{i_2} \cdot Y_{L_2} - K_{v_c}) \cdot Z_C) \cdot Y_{L_1}}$$

$$G_{d_{\text{AD}}}(s) = \frac{Y_{L_2} \cdot (1 + Y_{L_1} \cdot Z_C) + (K_{i_1} - (K_{v_c} + K_{v_s}) \cdot Z_C) \cdot Y_{L_2} \cdot Y_{L_1}}{1 + Z_C \cdot (Y_{L_1} + Y_{L_2}) + (K_{i_1} \cdot (1 + Z_C \cdot Y_{L_2}) + (K_{i_2} \cdot Y_{L_2} - K_{v_c}) \cdot Z_C) \cdot Y_{L_1}} \tag{10}$$

e_d is minimized) and the actuation signal u will be limited, respectively.

The exogenous inputs vector $\boldsymbol{w}$ is formed by the two disturbances to the damped plant, u_{AD} and v_s [see (9)]. In addition to feedforward these signals, $\mathbf{K}_{\text{AD}}$ will feedback some filter measurements, forming the vector $\boldsymbol{v}$. In Fig. 2, as well as in (8), (9), and (10), a complete states vector $\boldsymbol{x}$ feedback was considered to not lose generality. The method is, in any case, quite flexible and allows using one or several measurements of the grid filter (e.g., the grid current i_2) being only necessary in that case to modify the definition of the vector $\boldsymbol{v}$.

Plant $\mathbf{P}$ inputs and outputs are summarized as follows:

$$\boldsymbol{z} = \begin{bmatrix} W_d \cdot e_d \\ W_u \cdot u \end{bmatrix}, \quad \boldsymbol{v} = \begin{bmatrix} v_s \\ u_{\text{AD}} \\ \boldsymbol{x} \end{bmatrix}, \quad \boldsymbol{w} = \begin{bmatrix} v_s \\ u_{\text{AD}} \end{bmatrix}, \quad \boldsymbol{u} = u. \tag{13}$$

B. Reference Model and Weighting Function Selection

The design of the generalized plant $\mathbf{P}$ involves the selection of three transfer functions: The model-reference transfer function G_{ref} and the two involved weighting functions W_d and W_u.

G_{ref} is the way the designer specifies the damping strategy of the plant. This paper proposes to mimic an *L*-connection scenario, where the inductance and equivalent resistance match the addition of the actual *LCL*-filter inductances and resistances

$$G_{\text{ref}}(s) = \frac{1}{R_{\text{ref}} + sL_{\text{ref}}} = \frac{1}{(R_1 + R_2) + s(L_1 + L_2)}. \tag{14}$$

This transfer function closely resembles that of a damped version of the *LCL* one. Given the dipole nature of the *L*-filter, a single reference model is enough to shape both G_{AD} and $G_{d_{\text{AD}}}$ [defined in (10)], subtracting to that end u_{AD} from v_s, as it can be observed in Fig. 2 (purple color).

The objective of the W_d and W_u weighting functions is to specify the control bandwidth where the model is going to be emulated and, also, to limit the actuation level inside the control band to avoid undesired saturation in the plant actuator (maximum duty cycle, in this case).

W_d should be, thus, a low-pass filter, to emphasize the importance of e_d minimization (see Fig. 2) inside the control bandwidth. The proposed transfer function is

$$W_d(s) = K_d \frac{1}{(1/\omega_d)s + 1} \tag{15}$$

where K_d and w_d are constants that should be chosen to match the design objectives in emulation error and control bandwidth, respectively.

The design of W_u should be complementary: a high-pass filter, so outside of the control bandwidth the actuation is small. A possible choice is

$$W_u(s) = K_u \frac{(1/\omega_{u1})s + 1}{(1/\omega_{u2})s + 1}. \tag{16}$$

The bode plot of an example of both weighting function is shown in Fig. 3. Note the complementary nature of both functions. In practice, the design of the active damper depends on two factors: The relation between K_d and K_u, which will determine the shaping error minimization versus damper actuation limitation in the shaping band, and the cross frequency between W_d and W_u magnitudes, which will determine the shaping bandwidth. In the first case, a 40 dB difference (i.e., $K_d = 100K_u$) is usually enough to achieve a good shaping in the desired bands. As for the cross frequency, the only criterion is to select it to maximize the shaping bandwidth, which is limited, as it is explained in Section III-C, to approximately one sixth of the controller sampling frequency.

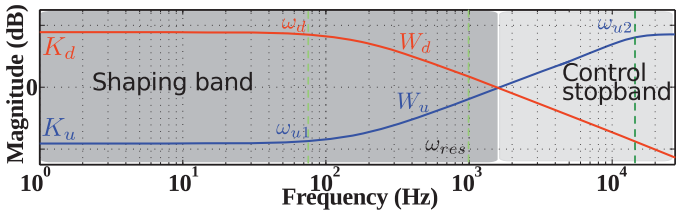

Fig. 3. Frequency representation of the considered weights W_d and W_u.

C. Controller Implementation and Limitations

The design procedure here proposed is subjected to several limitations. While some of them are inherent to any linear time invariant (LTI) control loop, other important limitations and considerations are due to the final sampled-data nature of the algorithm to be implemented.

1) Discrete-Time Implementation: $\mathcal{H}_\infty$ synthesis tools are designed to work in continuous-time scenarios. The controllers that have been proposed here will be coded and executed in a digital signal processor (DSP), and consequently, a discrete-time controller transfer function is needed. An approach that considers the problem to be continuous and after the synthesis obtains a discrete-time approximation of the controller neglects important dynamic components such as the presence of a PWM modulator, which may be modeled as a zero-order hold (ZOH), and the computational delay at the controller $\mathbf{K}_{\text{AD}}$ output (input to $\mathbf{G}$). Those modeling errors would induce inaccuracies in the model emulation that limit the performance of the synthesized controller, particularly in the neighborhood of Nyquist frequency. Those inaccuracies may be admissible in standard reference-tracking problems, but it is preferable to avoid them on this particular problem.

This paper uses the alternative approach described in [36]. The ZOH discrete-time equivalent of $\mathbf{G}(s)$ is computed and a one-sample delay z^{-1} is added to it in z domain. After introducing these dynamic elements in the process, a continuous approximation of this plant is obtained via bilinear transformation, making a frequency prewarping to accurately preserve *LCL* resonance frequency. $\mathbf{G}_d$ transfer matrix can be included directly into the generalized plant $\mathbf{P}(s)$ as the grid voltage is, in fact, a continuous disturbance to the process. An optimal continuous controller $\mathbf{K}_{\text{AD}}(s)$ is obtained through a regular $\mathcal{H}_\infty$ process. The final discrete-time controller $\mathbf{K}_{\text{AD}}(z)$ is, then, obtained by computing a Bilinear transformation.

A similar reasoning can be applied to the selection of the model-reference plant. As long as the ZOH and the delay exist in the plant under control, they would also exist in a hypothetical *L*-connection case that is used as the reference model. The

TABLE I
SETUP PARAMETERS

S_n	9 kVA	L_1	3.4 mH
V_g	120 V	R_1	28.8 mΩ
ω_1	$2\pi 60$ rad · s^{-1}	L_2	1.7 mH
V^*_{dc}	700 V	R_2	18.6 mΩ
T_s	200|100 μs	C	18 μF
T_{sw}	$2T_s$	C_{dc}	4.7 mF

synthesis process yields better results if the reference model is built following the same principles to include these dynamics.

Besides, the dynamic particularities derived from the sampled-data nature of the controller are also the cause of one fundamental limitation of the closed-loop system. The sampling frequency of the controller, together with the delay at the plant input, induces a limitation on the maximum achievable controller bandwidth f_c of

$$\omega_{c_{\text{MAX}}} = 2\pi f_{c_{\text{MAX}}} \approx \frac{1}{T_s} \text{ rad/s} \tag{17}$$

where T_s being the sampling period of the digital system [35]. It is important to remark that this bandwidth limitation affects to both feedback and feedforward paths. Good damping results cannot be assured, then, if the *LCL* resonance frequency f_{res} is above $f_{c_{\text{MAX}}}$. Consequently, the *LCL* resonance frequency imposes a minimum sampling and control frequency to achieve active damping. This is a classical theoretical limitation and affects to any sampled-data linear strategy to damp *LCL* filter resonance.

2) Weights Design Limitations: Elements in $\mathbf{P}$ must be strictly stable and proper. From a design point of view, it means that the defined weights cannot have pure integral/derivative terms or more zeros than poles. This limitations have, in any case, a very small influence in the controller performance, as it is possible to emulate pure integral/derivative terms by placing poles or zeros arbitrarily close to the $j\omega$ axis, and to make $\mathbf{P}$ proper by adding as many high-frequency poles as necessary.

In addition, it must be taken into account that the synthesized active-damping controller $\mathbf{K}_{\text{AD}}$ will have the same order of the generalized plant $\mathbf{P}$. This means that even though higher order frequency weights in $\mathbf{P}$ can be translated in a better damping performance, their definition will result in higher controller complexity and, then, higher computational times.

A more detailed explanation of a controller $\mathcal{H}_\infty$ synthesis and implementation, including the delays modeling and the final discrete controller obtaining, can be found in [36].

IV. RESULTS

This section analyses experimentally and numerically the validity of the proposed control procedure. Both cases assume a converter with the following parameters.

A. Validation Conditions

The main converter parameters used in numerical and experimental analysis are shown on Table I.

The study considers two different control sampling periods to better evaluate the influence of this parameter on controller design and performance.

1) Controller Location on Complete Control Loop: The controllers obtained using the proposed design procedure are not able to fully control the converter on their own, and need additional external control loops. These controllers have been chosen so they are as standard as possible.

The reference tracking is accomplished by a classical outer PR grid-current controller, designed for the *L*-equivalent filter reference in (14) [17]

$$K_{cc}(z) = K_p \left(1 + \frac{\sin(\omega_1 T_s)(z^2-1)}{T_r 2\omega_1 \left(z^2 - 2z\cos(\omega_1 T_s) + 1\right)}\right) \tag{18}$$

where the resonant time constant and the proportional gain are fixed for both sampling periods to $T_r = 0.004$ and $K_p = 12.648$, respectively. The controller bandwidth is the same, then, for both considered sampling periods. The resonant time constant T_r is chosen for a fast reference tracking. The proportional gain K_p is tuned so applying K_{cc} to the *LCL* filter (without damping) for a sampling period $T_s = 200$ μs results in a unstable system, but with stability margins close to zero. This is done to test the active-damping efficiency as a system stabilizer (see the test in Fig. 14).

Considering the damped *LCL* plant, the closed-loop dynamic of the controlled current i_2 follows the expression:

$$I_2 = \underbrace{\frac{G_{\text{AD}} \cdot K_{cc}}{1 + G_{\text{AD}} \cdot K_{cc}}}_{T(s)} I^* + \underbrace{\frac{G_{d_{\text{AD}}}}{1 + G_{\text{AD}} \cdot K_{cc}}}_{Y(s)} V_s \tag{19}$$

where $T(s)$ and $Y(s)$ are the closed-loop tracking and admittance transfer functions. The stability of the damped system can be obtained by means of LTI analysis of the loop function $L_{\text{AD}} = K_{cc} \cdot G_{\text{AD}}$. A perfect damping and improved stability margins would be obtained if L_{AD} is equal to its reference value $L_{\text{ref}} = -K_{cc} \cdot G_{\text{ref}}$. If the inner active-damping loop is not considered, L_{AD} would be equal to $L = K_{cc} \cdot F_{u \to i_2}$.

The considered application used for controller verification is an active PWM rectifier that needs a dc-voltage control loop. This outer loop consists of a standard PI-based control loop ($K_{\text{dc}}(z) = K_p + \frac{K_I T_s}{z-1}$, $K_p = 0.0992$, $K_I = 2.0742$), whose input is the difference between the dc-bus voltage reference and the measured value. Grid current references are computed from the K_{dc} controller output, together with the reactive power reference and the information extracted from grid PCC voltages.

2) Numerical Analysis and Simulation Platform: All numerical results shown on this section have been obtained using Mathworks MATLAB software tool. Simulation experiments have been performed using MATLAB Simulink tool, with the aid of SimPowerSystems (sub)library.

3) Experimental Platform: All experiments have been conducted on GEISER group facilities in Universidad de Alcalá.

Fig. 4 shows a picture of the experimental setup. It consist of an ac programmable power supply Pacific SmartSource 345-AMX, emulating the grid, and a two-level VSC of nominal power S_n connected to an *LCL* filter and a dc-bus capacitance

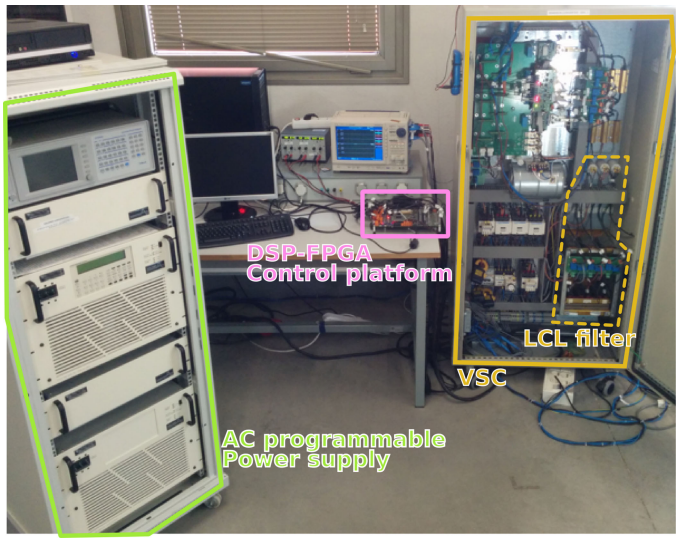

Fig. 4. Picture of the implemented experimental platform.

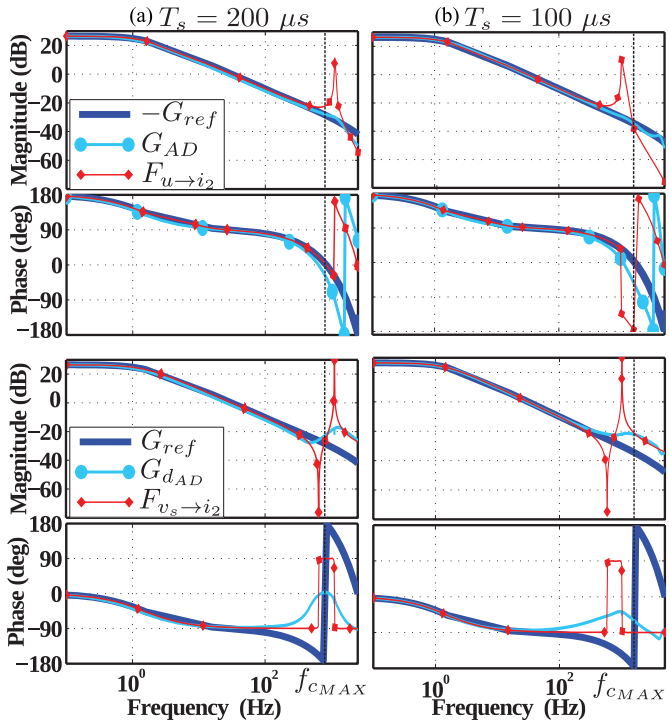

Fig. 5. *LCL* shaping results for the two different considered sampling periods, feeding back only i_2. Dynamic references (i.e., one of the *L*-filter) are represented in dark blue, the open-loop *LCL* dynamic is represented in red, and the obtained modified *LCL* dynamic is shown in light blue. Damping results improves for a smaller sampling period, thanks to the higher $\mathbf{K}_{\text{AD}}$ maximum bandwidth $f_{c\text{MAX}}$.

C_{dc}. Passive loads R_L are connected to the dc bus to test the platform under different operating points. Control algorithm is implemented on a Texas Instruments DSP TMS320DSK6713.

B. Damping Effectiveness Analysis

Fig. 5 shows the frequency-domain shaping (numerical) results of the synthesized controller for the two considered sampling periods, feeding back only the grid current i_2 (i.e.,

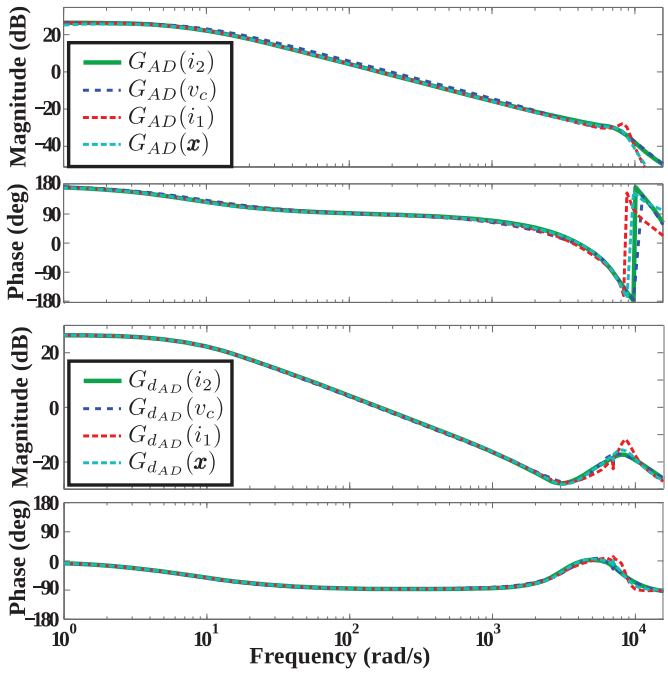

Fig. 6. Modified (i.e., damped) *LCL* dynamic considering different feedback loops: (green) only the grid current i_2 (dark blue) only the capacitor voltage v_c (red) only the converter current i_1 (light blue) the complete *LCL* filter states vector $\boldsymbol{x}$.

$\boldsymbol{x} = i_2$ in Fig. 2). As it can be seen, both modified *LCL*-filter dynamics, G_{AD} and $G_{d_{\text{AD}}}$, follow the *L*-filter reference G_{ref} damping the resonance of the unmodified *LCL*-filter dynamics, $F_{u\to i_2}$ and $F_{v_s\to i_2}$. Note that the proposed controller loses effectiveness around the maximum bandwidth $f_{c\text{MAX}}$ (i.e., all $\mathbf{K}_{\text{AD}}$ terms magnitude in (10) tend to zero, and so does its output u), so the modified *LCL* plant dynamics G_{AD} and $G_{d_{\text{AD}}}$ tend to zero and its open-loop value $F_{vs\to i_2}$, respectively. The results are better, then, for the smaller sampling period case $T_s = 100\ \mu$s, as the resonance frequency f_{res} is inside the achievable controller bandwidth. Damping results can be further improved for *LCL* filters with lower resonance frequencies and/or for lower implementation sampling periods.

Although the result shown in Fig. 5 corresponds to a design where only the grid current (i_2) is measured for the synthesized active damper, the design is flexible enough to achieve similar results feeding back any subset of the filter variables, as shown in Fig. 6. In it, the frequency-domain (numerical) results of the damped dynamics (G_{AD} and $G_{d_{\text{AD}}}$) are shown for a sampling period $T_s = 200\ \mu$s and different measured variables (identified in parentheses). Slightly worse results are obtained when only the converter current (i_1) is used. In any case, the results are very similar inside the active control band, before the band constraints described in Section III-C1.

For that reason, all the experiments and conclusions reported on the rest of this section have been obtained using a damping controller that only uses the grid current i_2 and voltage v_s as measured variables because it is considered the most interesting case in most applications.

Fig. 7 shows different numerical open-loop functions, and their deduced stability margins, when the designed grid-current

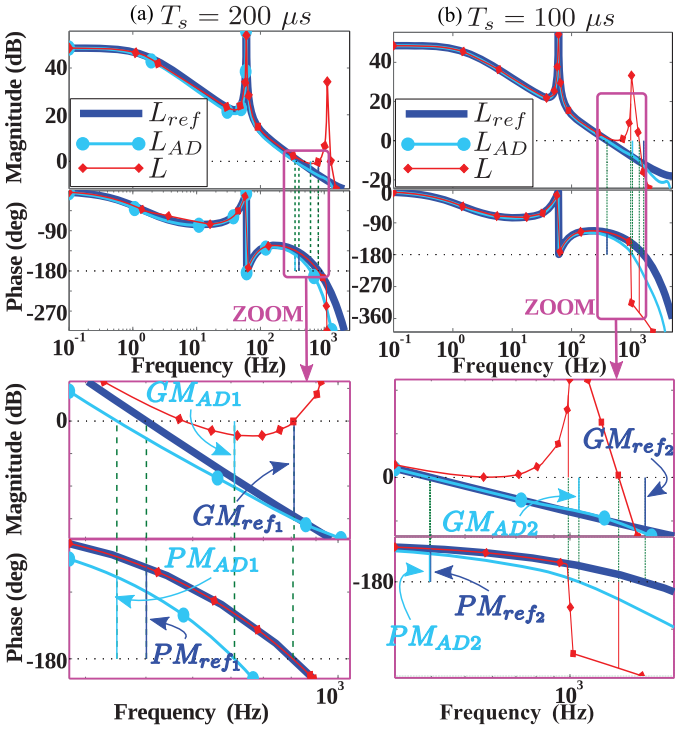

Fig. 7. Open-loop function frequency response numerical representation for the unmodified *LCL* filter (red), the reference *L*-filter (dark blue), and the modified *LCL* filter (light blue). Their corresponding stability margins are detailed in Table II.

TABLE II
STABILITY MARGINS FOR $T_s = 200\ \mu$S (TOP) AND $T_s = 100\ \mu$S (BOTTOM)

	No AD	AD	ref	$\frac{\text{AD}}{\text{ref}}$
PM_1	$-0.31°$	$36.8°$	$41.3°$	0.891
GM_1	0.05 dB	4.07 dB	5.86 dB	0.694
PM_2	$44.3°$	$58.4°$	$63°$	0.927
GM_2	-17.2 dB	8.9 dB	12 dB	0.741

controller K_{cc} is applied to the damped *LCL* plant G_{AD} (see L_{AD}), applied to the *L*-filter reference G_{ref} (see L_{ref}), and applied to the unmodified *LCL* plant $F_{u\to i_2}$ (see L). As stated before, K_{cc} is designed to be unstable if applied to the unmodified *LCL* plant with a sampling period $T_s = 200\ \mu$s, with gain GM and phase PM margins close to zero (see GM_1 and PM_1 in Table II). K_{cc} is again designed for a sampling period $T_s = 100\ \mu$s, following (18), with the same design parameters K_p and T_r. This will result in a clearly unstable system if it is directly applied to the undamped plant (see GM_2 and PM_2 in Table II).

Designed damping controller stabilizes both cases. Table II summarizes the achieved stability margins seen in Fig. 7. In it, subindex AD and ref stands for the damped *LCL*-filter case (loop L_{AD}) and the *L*-filter reference case (loop L_{ref}), respectively, meanwhile the sampling periods $T_s = 200\ \mu$s and $T_s = 100\ \mu$s are identified by subindex 1 and 2, respectively. Both designed controllers increase stability margins almost to their respective reference values, with better results for the smaller sampling

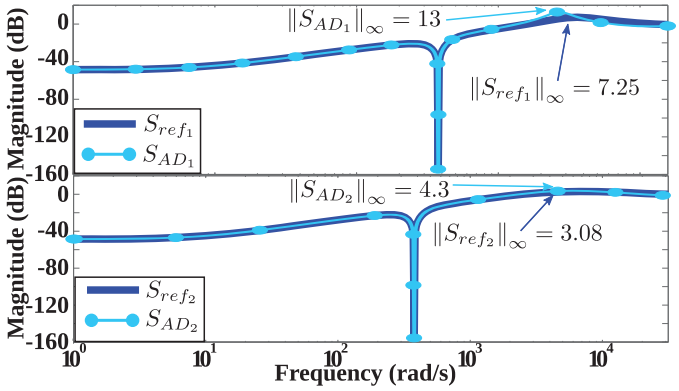

Fig. 8. Comparison between the sensitivity transfer functions of the reference *L*-filter system (S_{ref}) and the damped *LCL*-filter system (S_{AD}) for the two sampling periods considered (Upper: $T_s = 200\ \mu$s, lower: $T_s = 100\ \mu s$.)

period design, as can be seen in the rightmost column that shows a performance index that compares the achieved stability margins to its reference values.

The improvement of the system stability robustness when the sampling period (T_s) is reduced is further demonstrated in the sensitivity functions comparison between the reference *L*-filter dynamic ($S_{\text{ref}} = (1 + L_{\text{ref}})^{-1}$) and the damped *LCL*-filter dynamic ($S_{\text{AD}} = (1 + L_{\text{AD}})^{-1}$) shown in Fig. 8. As it can be seen, the maximum sensitivity gain of the actively damped design ($\|S_{\text{AD}_2}\|_\infty$) decreases when the sampling period is reduced to $T_s = 100\ \mu$s, being its value much closer to its reference at that sampling period ($\|S_{\text{ref}_2}\|_\infty$).

Fig. 9 shows the closed-loop input admittance frequency response results of the considered system (a) without the proposed active damping and (b) with the proposed active damping for a sampling period $T_s = 200\ \mu$s. The purple line represents the numerical value of the obtained admittance (Y), whose dynamic was defined in (19), meanwhile red circles represents experimental identified values of it (Y_{exp}) taken at different frequencies.[2] The resonance in the *LCL* open-loop admittance ($F_{vs\to i_2}$), in black, is highly damped with $\mathbf{K}_{\text{AD}}$ connected, but it is not with $\mathbf{K}_{\text{AD}}$ disconnected,[3] as can be deduced from the experimental results.

Fig. 10 repeats the results shown in Fig. 9, this time for a reduced sampling period $T_s = 100\ \mu$s. In this case, the undamped system is unstable in the experimental platform (as predicted theoretically, see GM_2 and PM_2 in Table II), not allowing to measure experimentally the obtained closed-loop admittance. Fig. 10 shows, then, only the results when the proposed active damping ($\mathbf{K}_{\text{AD}}$) is connected. As it can be seen, the *LCL*-filter

[2]To do so, the system is excited with PCC disturbances at different frequencies, thanks to the grid simulator. The grid current response at each frequency is then measured. The relations between excitations and responses, in both phase and amplitude, give the experimental admittance values Y_{exp}.

[3]The undamped system (i.e., with $\mathbf{K}_{\text{AD}}$ disconnected) considering a $T_s = 200\ \mu$s is stable in the tested experimental platform, even though it is not theoretically (see GM_1 and PM_1 in table II), allowing to measure the experimental admittance (Y_{exp}) shown in Fig. 9(a). That is probably due to the more damped experimental behavior of the system (compare Y_{exp} and Y phase around the resonant frequency).

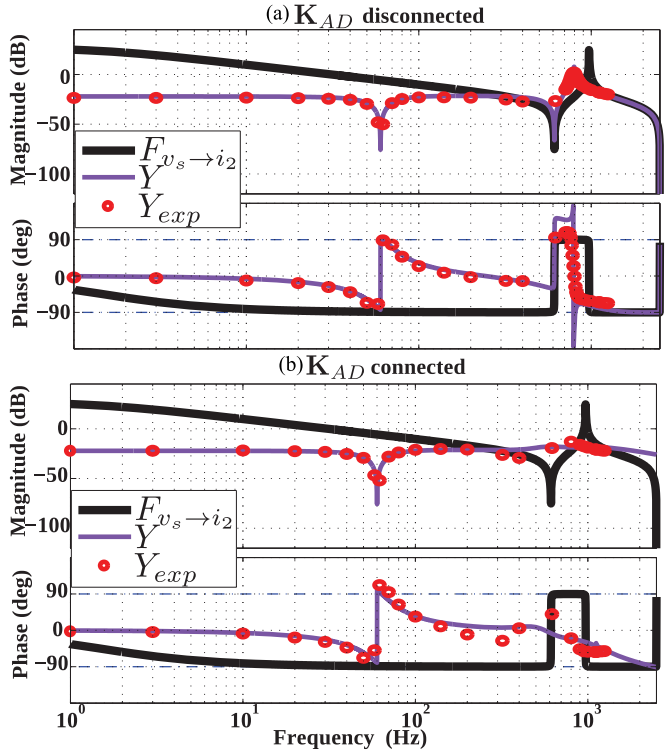

Fig. 9. Closed-loop numerical and experimental admittance frequency response for $T_s = 200\ \mu$s: (a) without the proposed active damping and (b) with the proposed active damping.

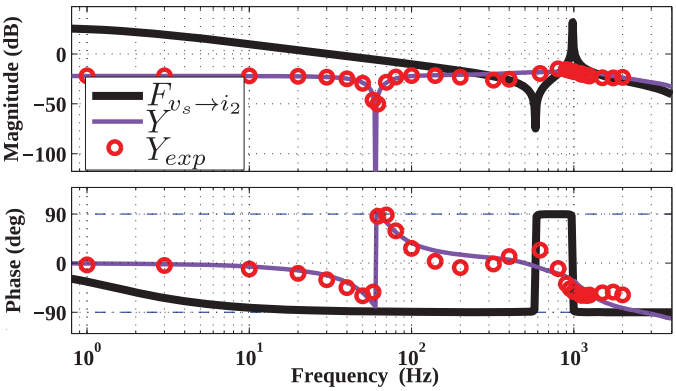

Fig. 10. Closed-loop numerical and experimental admittance frequency response for $T_s = 100\ \mu$s and $\mathbf{K}_{\mathrm{AD}}$ connected.

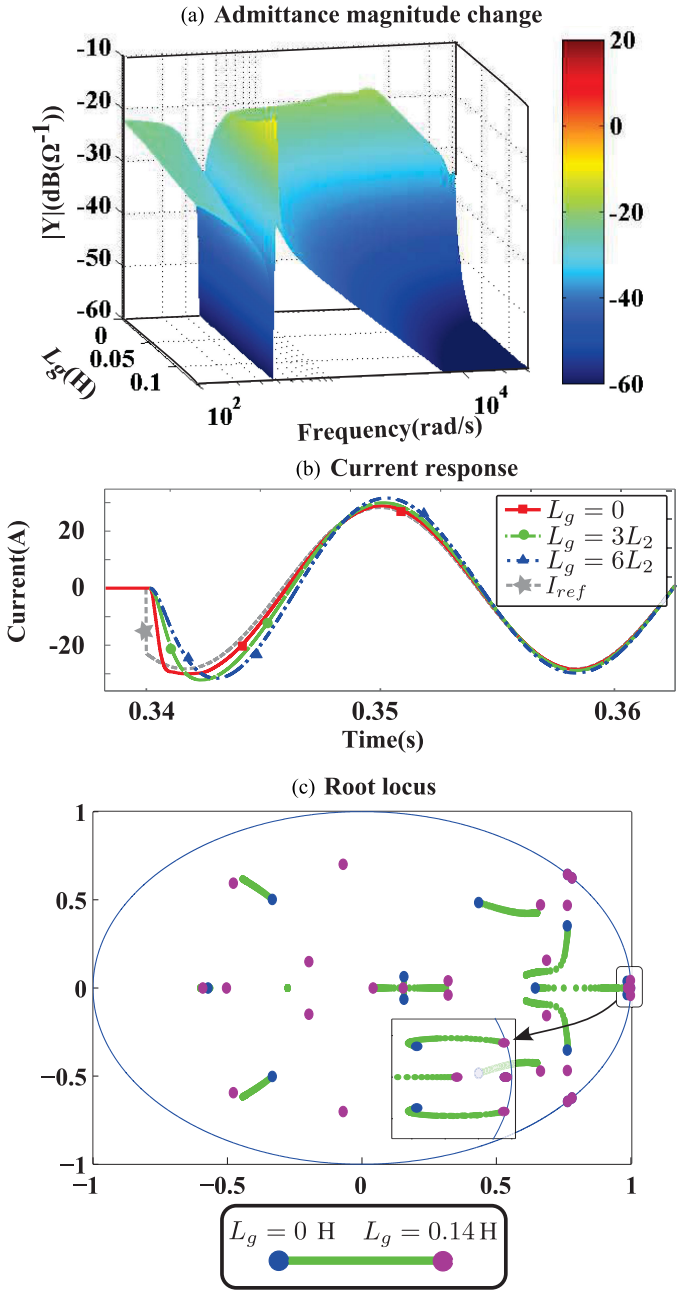

Fig. 11. Analysis of the effect of L_g perturbation. (a) Expected admittance frequency response magnitude, (b) current time response, and (c) closed-loop poles positions for changes of an inductive grid $Z_g = L_g s$.

resonance (see $F_{vs \to i_2}$) is slightly better damped experimentally for this reduced sampling period.

Closed-loop input admittance is an important indicator of active-damping performance as it specifies how the converter is going to react in the presence of grid disturbances, predicting possible oscillations or instability situations.

C. Robustness Analysis

The grid impedance (Z_g in Fig. 1) seen by the converter from the PCC is usually unknown to a great extent. Particularly, the uncertainty associated with its inductance L_g is perhaps the main practical concern regarding converter closed-loop robustness and a potential source of cost increase due to maintenance and converter unavailability. Fig. 11 summarizes the robustness analysis, showing (a) the (numerical) closed-loop admittance frequency response magnitude, (b) the current time response, and (c) the trajectories of the system closed-loop poles for variations of an inductive grid impedance $Z_g = L_g s$. As it can be seen, the system is well damped and stable for all possible variations of the grid inductance between $L_g = [0, 0.14]$ H.

Fig. 12 shows the damping robustness of the method toward parametric variations of the *LCL* filter. It represents, in the top, the closed-loop frequency response of the expected (numerical) admittance magnitude ($|Y|$) for changes of the *LCL* parameters L_1, L_2, and C. High (resonant) values of $|Y|$ in Fig. 12 would

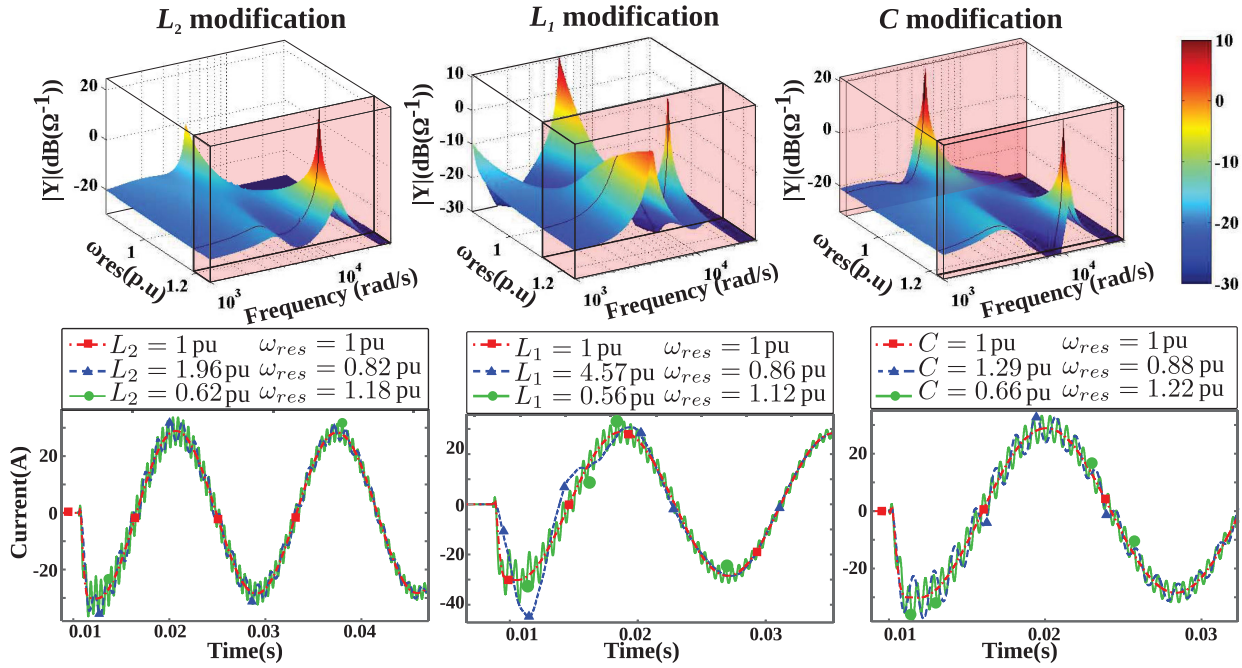

Fig. 12. (Top) Expected admittance magnitude modification for changes of the *LCL* resonance frequency. High (resonant) values would indicate ineffective action of the designed active damping. Red boxes represent unstable cases. (Bottom) Grid current response to a reference change for different values of the filter parameters.

indicate ineffective action of the designed active damping. A sampling period of $T_s = 100$ μs was considered for the grid-current controller (K_{cc}) and the damping controller ($\mathbf{K}_{\text{AD}}$) designs. Then, the resonance frequency (ω_{res}) is changed from 0.85 to 1.25 p.u. of its nominal value by modifying each of the *LCL* elements. $|Y|$ in Fig. 12 for $\omega_{\text{res}} = 1$ p.u. is, then, equivalent to $|Y|$ in Fig. 10. The red boxes represent resonance frequency limits from which the system becomes unstable. In addition, the bottom part of Fig. 12 shows the simulated time-domain response of the controlled current for the nominal filter and for stable variations of each filter parameter. The system is stable for the next variations of the filter parameters: $L_1 = [8.23,\ 0.56]$ p.u.,[4] $L_2 = [2.03,\ 0.62]$ p.u., and $C = [1.32,\ 0.66]$ p.u.; well above the expected tolerance on commercial filter inductances and capacitors, which is usually within $\pm 10\%$. To further demonstrate the robustness of the system, the top part of Fig. 13 shows the obtained closed-loop admittance for the nominal filter (see Y), for the worst damping case (i.e., larger $\|Y\|_\infty$) considering filter parameters within a tolerance of $\pm 10\%$ and the considered L_g uncertainty range (see Y_{wc}), and for this worst case scenario but with a nonideal grid impedance (see Y_{wcL_g}). In addition, the bottom part of the figure shows the (simulated) current response to a reference change for the aforementioned cases. As it can be seen, the damping results for the worst filter parameters[5] are still enough to result in small oscillations in the controlled current. It is also important to remark that a nonzero grid inductance modifies the filter resonance frequency but does not worsen the damping performance.

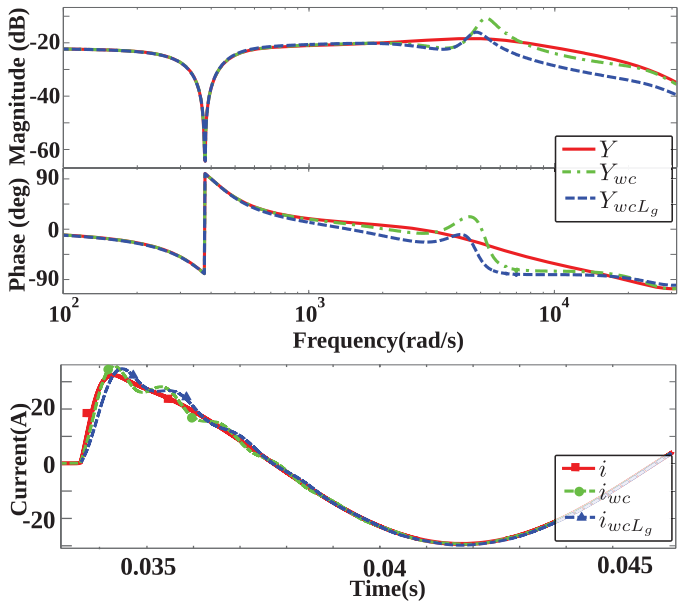

Fig. 13. Closed-loop admittance and current response to a reference change; (red) for the nominal filter conditions and an ideal grid impedance; (dashed green) for the worst filter case, in terms of resonance damping, with a parameters tolerance of $\pm 10\%$ and an ideal grid impedance; and (dashed blue) for the worst filter case and a nonideal grid (dashed blue).

D. Time-Domain Results

Fig. 14 shows simulated time-domain results of the performance of the designed active damping ($\mathbf{K}_{\text{AD}}$) for a $T_s = 200$ μs.

[4]The nominal value of the filter resonance is $\omega_{\text{res}N} = \sqrt{(L_{1N} + L_{2N})/(L_{1N} L_{2N} C_N)} \approx 7000$ rad/s, where L_{1N}, L_{2N}, and C_N are the filter nominal parameters shown in Table I.

[5]The worst damping case for variations of the filter parameters within the considered tolerance are $C = 1.1$ p.u., $L_1 = 1.1$ p.u., and $L_2 = 1.1$ p.u.

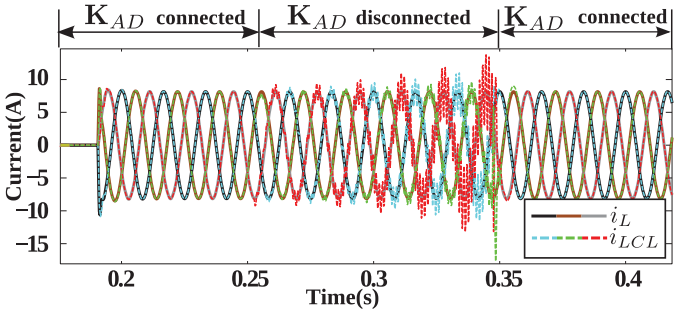

Fig. 14. Simulated time-domain active-damping results. i_{abcL} and i_{abcLCL} represent the grid current for the emulated *L*-filter and the considered *LCL* filter, respectively. Both are equivalent if $\mathbf{K}_{\mathrm{AD}}$ is connected. An unstable oscillation grows if $\mathbf{K}_{\mathrm{AD}}$ is disconnected. This oscillation is quickly dissipated if $\mathbf{K}_{\mathrm{AD}}$ is again connected.

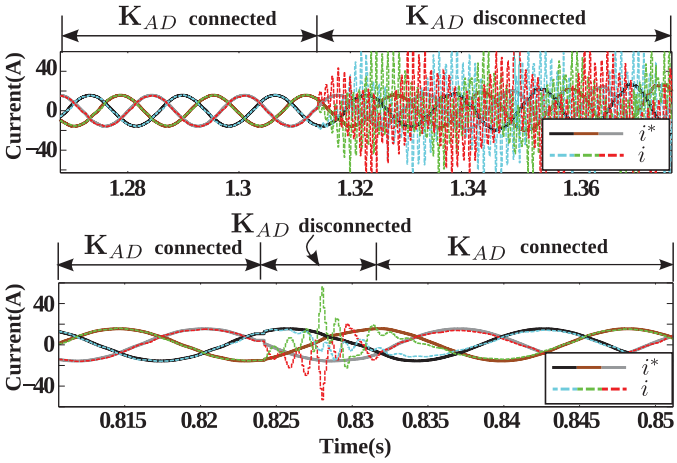

Fig. 15. Experimental time-domain results of the controlled current with and without the proposed active damper for a $T_s = 100\ \mu$s.

Two applications were simulated simultaneously to obtain these results: One VSC connected to the grid through the equivalent *L*-filter, controlling its grid current (i_L) with only the proposed external current controller (K_{cc}), and another VSC connected to the same grid through the considered *LCL* filter, controlling its current (i_{LCL}) with the proposed active damper ($\mathbf{K}_{\mathrm{AD}}$) and the aforementioned outer current controller (K_{cc}). The response of the *LCL*-filter grid current (i_{LCL}) is very similar to one of the emulated *L*-filter (i_L), demonstrating the good dynamics shaping achieved with $\mathbf{K}_{\mathrm{AD}}$. It can be seen how the grid current of the *LCL* filter (i_{LCL}) starts to oscillate at the resonant frequency if $\mathbf{K}_{\mathrm{AD}}$ is disconnected. If $\mathbf{K}_{\mathrm{AD}}$ is connected again, this oscillation is quickly dissipated.

Fig. 15 shows the experimental evolution of a controlled system under K_{AD} different connection status. The top of the figure shows how the current becomes unstable if $\mathbf{K}_{\mathrm{AD}}$ is disconnected during a long period. The bottom of the figure shows a short-period $\mathbf{K}_{\mathrm{AD}}$ disconnection. As it can be seen, connecting again $\mathbf{K}_{\mathrm{AD}}$ will stabilize the system.

Figs. 16 to 18 show experimental results of the implemented damped *LCL* grid current control at sampling period $T_s = 100\ \mu$s for different tests: Fig. 16 shows the response to

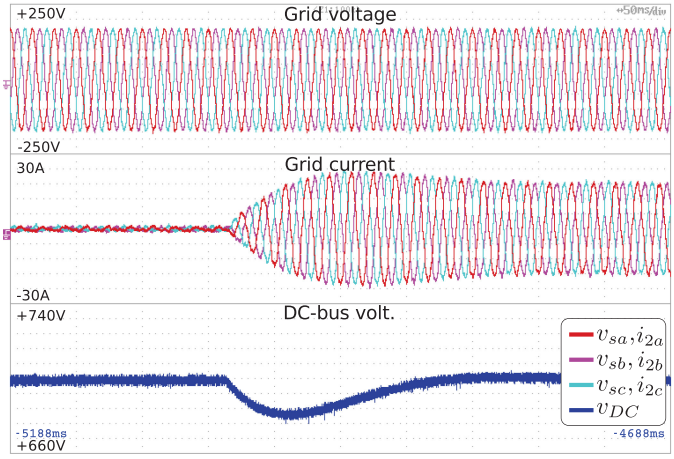

Fig. 16. Connection of a 4.2 kW dc load with a null reactive reference. The grid current increases to supply the dc load, maintaining the dc-bus voltage v_{dc} constant.

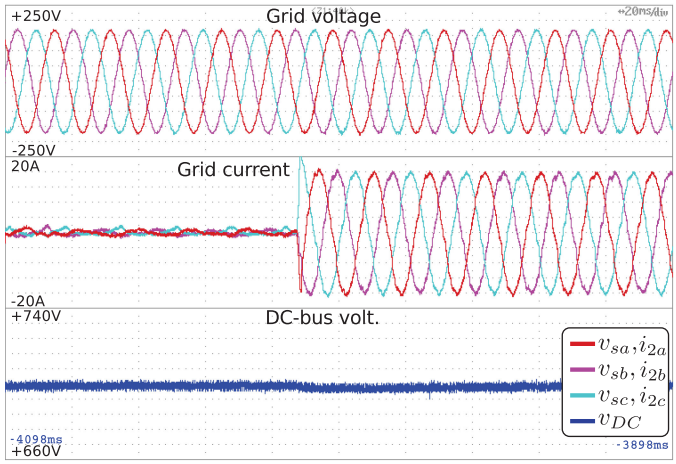

Fig. 17. Sudden change to a reactive power reference of $q^* = 4$ kvar with a null active power reference. The grid current quickly track the new reactive power demand.

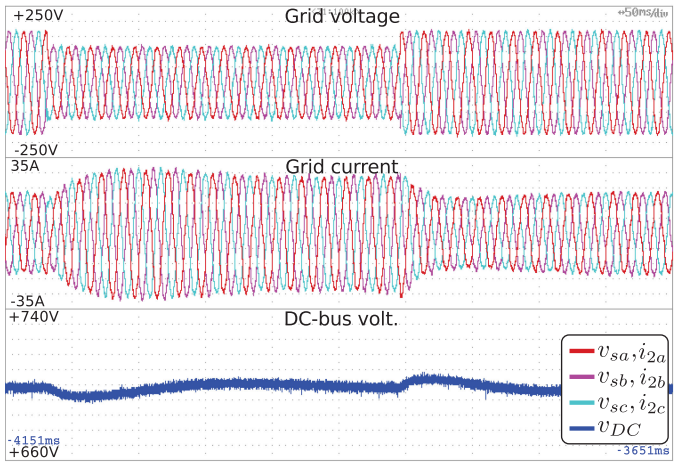

Fig. 18. Initial response and recovery to a balanced grid voltage dip of 70%. The system is supplying a load of $P = 4.2$ kW. The grid current increased to compensate the power interchange decrease during the voltage dip.

a change of the passive dc-load power demand from $P = 0$ to $P = 4.2$ kW, Fig. 17 shows the results of a sudden change of the reactive power reference from $Q^* = 0$ to $Q^* = 4$ var, and Fig. 18 shows the response of the system to a balanced grid voltage dip of 70% of its nominal value (with a load of $P = 4.2$ kW). Damped system is proven to be quick and stable for all the aforementioned tests.

E. Performance Comparison With Related Classic Approaches

The performance of the proposed method is compared with the main two classical approaches to active damping that only measure one current to reduce the number of sensors needed: The notch filter approach [15], [22], [23] and the high-pass filter—lead-lag network [21]. Both proposals have been long studied in literature. Authors have selected the most recent relevant articles on both approaches.

The dynamic of these two elements in the Laplace domain are as follows:

$$\text{Notch}(s) = \left(\frac{s^2 + 2D_z\omega_{nf}s + \omega_{nf}^2}{s^2 + 2D_p\omega_{nf}s + \omega_{nf}^2} \right)^n \tag{20}$$

$$\text{HPF}(s) = \frac{k_{\text{HPF}}s}{s + \omega_{\text{HPF}}}. \tag{21}$$

The notch filter, Notch, is placed in series to the outer current controller [equivalent to: $K_u = \text{Notch}(s)$, $K_{v_s} = 0$, $K_{i_2} = 0$, $K_{v_c} = 0, K_{i_1} = 0$ in (8)], selecting $\omega_{nf} = \omega_{\text{res}}$ to avoid feeding the filter resonance with the VSC output voltage, but still actuating at the rest of frequencies. D_z is usually selected equal to zero, resulting in $|\text{Notch}(j\omega)| = 0$ at $\omega = \omega_{\text{res}}$. D_p will control the notch bandwidth: The wider is this bandwidth, the more robust the notch will be to variations of the filter resonance, affecting, in turn, other low control frequencies. In that regard, increasing the notch order n makes possible to increase the notch bandwidth without affecting so much other frequencies, increasing in turn the computational complexity of the damper. As it shown in [23], a good compromise is to select $n = 2$.

The high-pass filter $\text{HPF}(s)$ has two parameters: ω_{HPF} and k_{HPF}, which represent its bandwidth and maximum gain, respectively. This filter will feedback the grid current i_2 to modify the outer current controller output [i.e., similar to set $K_{i2} = -\text{HPF}$ in the proposed damper $\mathbf{K}_{\text{AD}}$, with all its other terms set to zero in (8)].

The optimal design of these two proposals is usually based on the analysis of the resonant closed-loop poles trajectories for variations of their design parameters. Considering the notch filter, this process is relatively simple, as in practice it only depends on the optimal selection of D_p. On the other hand, the selection of optimal values for the high-pass filter is more complicated, not only because in this case the two design parameters affect the obtained performance, but also because their variation not always follow a *predictable* effect on the poles trajectories, depending on other factors as the sampling and resonant frequencies [21]. Moreover, the performance of the notch filter and the high-pass filter strongly depends on the design of the outer current controller, mainly on its bandwidth [21], [23].

Figs. 19 and 20 show, on the top, the frequency-domain response of the admittance (Y) and tracking (T) closed-loop transfer functions, respectively, when the proposed PR outer current controller (K_{cc}) is implemented with a sample period $T_s = 100$ μs, damping the filter resonance with the proposed damper ($\mathbf{K}_{\text{AD}}(s)$), the notch filter ($\text{Notch}(s)$), and the high-pass filter ($\text{HPF}(s)$). In addition, the bottom part of Figs. 19 and 20 show the time-domain response of the grid current to a PCC voltage (v_s) dip and a current reference (i^*) change, respectively, for the three aforementioned methods. The design criterion for the two considered damping filters is similar and based on the analysis of the root locus of the system loop for variations of a proportional outer current controller (i.e., setting $K_{cc} = K_p$). The design parameters are then selected so the system is as robust as possible to variations of K_p, which usually results in a better damping of the filter resonance.

As it can be seen in Figs. 19 and 20 results, the proposed method shows a better performance than the previous approaches for the predesigned PR controller (K_{cc}). Fig. 19 needs

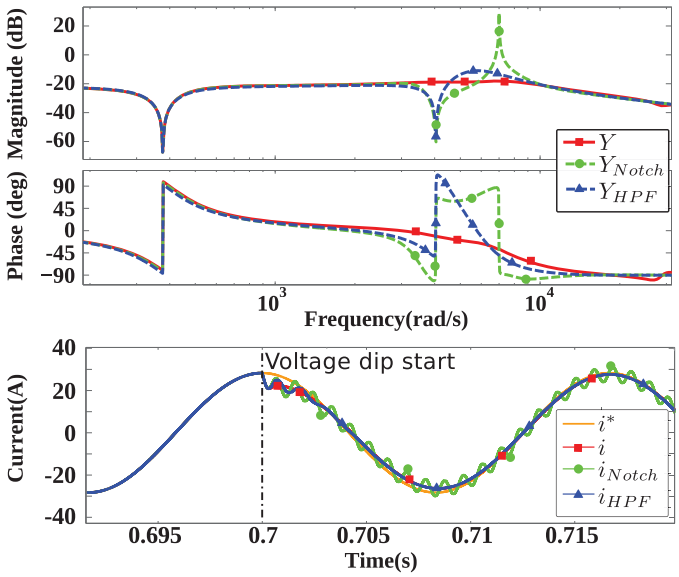

Fig. 19. Comparison of the closed-loop admittance (Y) and the current (i) response to a PCC voltage (v_s) dip for the proposed active damper (red), the notch filter (green), and the high-pass filter (blue).

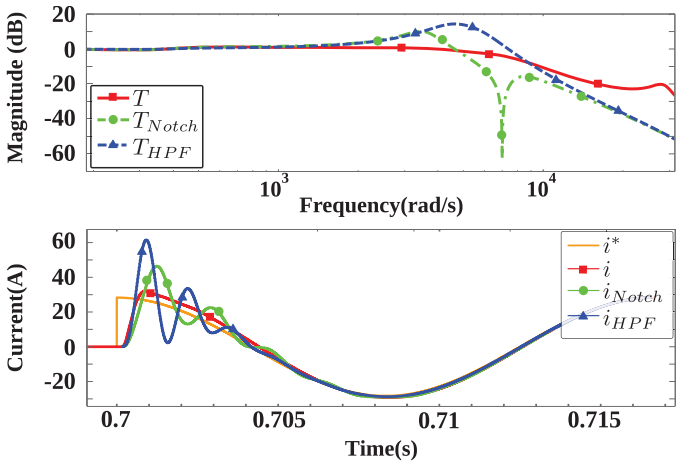

Fig. 20. Comparison of the closed-loop admittance (Y) and the current (i) response to a current reference (i^*) change for the proposed active damper (red), the notch filter (green), and the high-pass filter (blue).

particular attention due to the small damping that is achieved with notch-based active damping in the closed-loop admittance transfer function. This translates, as shown in Fig. 19, in a long oscillating transient in the voltage dip response. Nevertheless these oscillations eventually vanish and current reference tracking is never compromised. Additionally, Y_{HPF} suffers from steep phase shifts that may compromise the system passivity and, then, its stability with weak grids [33]. On the other hand, Fig. 20 shows that both damping filters have a larger overshoot than the proposed method for variations of the current reference (i^*) due to their smaller damping.

It can be concluded that even though the proposed active damper may have a bigger computational design complexity than previous active-damping proposals, it is compensated with the improvement in the performance and clearness for outer controller design.

Besides, the design of this proposal is mainly based on the selection of two simple frequency-domain weights that besides the control bandwidth (dependent of controller sampling frequency) does not depend on the *LCL*-filter parameters (e.g., its resonance frequency) or the outer current controller to achieve the optimal performance. This could make the proposal valid for its implementation on a systematic tool with possible industry uses.

V. Conclusion

This paper has presented an active-damping controller design for *LCL*-filter grid-connected VSC. It modifies grid-current dynamic in order to mimic one of the equivalent *L*-filter, making possible the use of simple PI or PR controllers to track the desired current with minimum stability and performance penalties.

Proposed controller is obtained by (sub)optimal $\mathcal{H}_\infty$ synthesis following a model-reference design. The designer specifies the desired *LCL* grid-current dynamic, in this case one equivalent to an *L*-filter. The synthesis algorithm obtains, then, an optimal controller that complies with the specifications, resulting in a damped system. Design methodology is flexible enough to specify the number of inputs to the controller, considering different *LCL* or disturbances measurements, increasing its suitability for industry configurations. Limitations of the method are presented, being the most important a bandwidth limitation coming from the discrete-time implementation of the controller.

Obtained frequency-domain results show the damping capabilities of the presented method. Stability margins are, then, minimally decreased if an *L*-filter predesigned grid-current controller is applied to the modified *LCL* filter. In addition, damping and stability robustness of the method is proved for variations of the *LCL* filter and the grid impedance parameters. Finally, good time-domain results are demonstrated by experimental tests. Damping performance of the method has been compared, with positive results, with related existing methods.

References

[1] J. Dannehl, F. W. Fuchs, S. Hansen, and P. B. Thøgersen, "Investigation of active damping approaches for PI-based current control of grid-connected pulse width modulation converters with LCL filters," *IEEE Trans. Ind. Appl.*, vol. 46, no. 4, pp. 1509–1517, Jul./Aug. 2010.

[2] M. Liserre, R. Teodorescu, and F. Blaabjerg, "Stability of photovoltaic and wind turbine grid-connected inverters for a large set of grid impedance values," *IEEE Trans. Power Electron.*, vol. 21, no. 1, pp. 263–272, Jan. 2006.

[3] L. Harnefors, L. Zhang, and M. Bongiorno, "Frequency-domain passivity-based current controller design," *IET Power Electron.*, vol. 1, no. 4, pp. 455–465, 2008.

[4] B. Bahrani, M. Vasiladiotis, and A. Rufer, "High-order vector control of grid-connected voltage-source converters with LCL-filters," *IEEE Trans. Ind. Electron.*, vol. 61, no. 6, pp. 2767–2775, Jun. 2014.

[5] F. Huerta, D. Pizarro, S. Cóbreces, F. J. Rodriguez, C. Giron, and A. Rodriguez, "LQG servo controller for the current control of LCL grid-connected voltage-source converters," *IEEE Trans. Ind. Electron.*, vol. 59, no. 11, pp. 4272–4284, Nov. 2012.

[6] J. Kukkola, M. Hinkkanen, and K. Zenger, "Observer-based state-space current controller for a grid converter equipped with an LCL filter: Analytical method for direct discrete-time design," *IEEE Trans. Appl.*, vol. 51, no. 5, pp. 4079–4090, Sep. 2015.

[7] R. Guzman, L. G. de Vicuña, J. Morales, M. Castilla, and J. Miret, "Model-based active damping control for three-phase voltage source inverters with LCL filter," *IEEE Trans. Power Electron.*, vol. 32, no. 7, pp. 5637–5650, Jul. 2017.

[8] M. Liserre, F. Blaabjerg, and S. Hansen, "Design and control of an LCL-filter-based three-phase active rectifier," *IEEE Trans. Ind. Appl.*, vol. 41, no. 5, pp. 1281–1291, Sep./Oct. 2005.

[9] R. D. Middlebrook, "Input filter considerations in design and application of switching regulators," *Proc. Conf Rec. Annu. Meet. Ind. Appl. Soc.*, 1976, pp. 366–382.

[10] R. Pena-Alzola, M. Liserre, F. Blaabjerg, R. Sebastián, J. Dannehl, and F. W. Fuchs, "Analysis of the passive damping losses in LCL-filter-based grid converters," *IEEE Trans. Power Electron.*, vol. 28, no. 6, pp. 2642–2646, Jun. 2013.

[11] R. W. Erickson, "Optimal single resistor damping of input filters," in *Proc. Appl. Power Electron. Conf. Expo.*, 1999, vol. 2, pp. 1073–1079.

[12] M. Liserre, A. Dell'Aquila, and F. Blaabjerg, "Stability improvements of an LCL-filter based three-phase active rectifier," in *Proc. 33th Annu. IEEE Power Electron. Spec. Conf.*, 2002, vol. 3, pp. 1195–1201.

[13] V. Blasko and V. Kaura, "A novel control to actively damp resonance in input LC filter of a three-phase voltage source converter," *IEEE Trans. Ind. Appl.*, vol. 33, no. 2, pp. 542–550, Mar./Apr. 1997.

[14] E. Wu and P. W. Lehn, "Digital current control of a voltage source converter with active damping of LCL resonance," in *Proc. 20th Annu. IEEE Appl. Power Electron. Conf. Expo.*, 2005, vol. 3, pp. 1642–1649.

[15] J. Dannehl, M. Liserre, and F. W. Fuchs, "Filter-based active damping of voltage source converters with filter," *IEEE Trans. Ind. Electron.*, vol. 58, no. 8, pp. 3623–3633, Aug. 2011.

[16] J. He and Y. W. Li, "Generalized closed-loop control schemes with embedded virtual impedances for voltage source converters with LC or LCL filters," *IEEE Trans. Power Electron.*, vol. 27, no. 4, pp. 1850–1861, Apr. 2012.

[17] S. G. Parker, B. P. McGrath, and D. G. Holmes, "Regions of active damping control for LCL filters," *IEEE Trans. Ind. Appl.*, vol. 50, no. 1, pp. 424–432, Jan./Feb. 2014.

[18] Y. Tang, P. C. Loh, P. Wang, F. H. Choo, and F. Gao, "Exploring inherent damping characteristic of LCL-filters for three-phase grid-connected voltage source inverters," *IEEE Trans. Power Electron.*, vol. 27, no. 3, pp. 1433–1443, Mar. 2012.

[19] J. L. Agorreta, M. Borrega, J. López, and L. Marroyo, "Modeling and control of-paralleled grid-connected inverters with LCL filter coupled due to grid impedance in PV plants," *IEEE Trans. Power Electron.*, vol. 26, no. 3, pp. 770–785, Mar. 2011.

[20] C. A. Busada, S. G. Jorge, and J. A. Solsona, "Full-state feedback equivalent controller for active damping in LCL-filtered grid-connected inverters using a reduced number of sensors," *IEEE Trans. Ind. Electron.*, vol. 62, no. 10, pp. 5993–6002, Oct. 2015.

[21] X. Wang, F. Blaabjerg, and P. C. Loh, "Grid-current-feedback active damping for LCL resonance in grid-connected voltage-source converters," *IEEE Trans. Power Electron.*, vol. 31, no. 1, pp. 213–223, Jan. 2016.

[22] M. Liserre, A. D. Aquila, and F. Blaabjerg, "Genetic algorithm-based design of the active damping for an LCL-filter three-phase active rectifier," *IEEE Trans. Power Electron.*, vol. 19, no. 1, pp. 76–86, Jan. 2004.

[23] R. Peña-Alzola, M. Liserre, F. Blaabjerg, M. Ordonez, and T. Kerekes, "A self-commissioning notch filter for active damping in a three-phase LCL-filter-based grid-tie converter," *IEEE Trans. Power Electron.*, vol. 29, no. 12, pp. 6754–6761, Dec. 2014.

[24] M. Orellana and R. Griñó, "On the stability of discrete-time active damping methods for VSI converters with a LCL input filter," in *Proc. 38th Annu. Conf. IEEE Ind. Electron. Soc.*, 2012, pp. 2378–2383.
[25] M. Cespedes, L. Xing, and J. Sun, "Constant-power load system stabilization by passive damping," *IEEE Trans. Power Electron.*, vol. 26, no. 7, pp. 1832–1836, Jul. 2011.
[26] H. Mosskull, "Optimal stabilization of constant power loads with input LC-filters," *Control Eng. Practice*, vol. 27, pp. 61–73, 2014.
[27] Q.-C. Zhong and T. Hornik, *Control of Power Inverters in Renewable Energy and Smart Grid Integration*, vol. 97. Hoboken, NJ, USA: Wiley, 2012.
[28] T. Hornik and Q.-C. Zhong, "Parallel PI voltage H-inf current controller for the neutral point of a three-phase inverter," *IEEE Trans. Ind. Electron.*, vol. 60, no. 4, pp. 1335–1343, Apr. 2013.
[29] G. Weiss, Q.-C. Zhong, T. C. Green, and J. Liang, "H-inf repetitive control of DC-AC converters in microgrids," *IEEE Trans. Power Electron.*, vol. 19, no. 1, pp. 219–230, Jan. 2004.
[30] S. Cóbreces, E. J. Bueno, F. J. Rodriguez, D. Pizarro, and F. Huerta, "Robust loop-shaping H-inf control of LCL-connected grid converters," in *Proc. IEEE Int. Symp. Ind. Electron.*, 2010, pp. 3011–3017.
[31] R. Naim, G. Weiss, and S. Ben-Yaakov, "H-inf control applied to boost power converters," *IEEE Trans. Power Electron.*, vol. 12, no. 4, pp. 677–683, Jul. 1997.
[32] T.-S. Lee, S. Chiang, and J.-M. Chang, "H-inf loop-shaping controller designs for the single-phase ups inverters," *IEEE Trans. Power Electron.*, vol. 16, no. 4, pp. 473–481, Jul. 2001.
[33] L. Harnefors, X. Wang, A. Yepes, and F. Blaabjerg, "Passivity-based stability assessment of grid-connected VSCs—An overview," *IEEE J. Emerg. Sel. Topics Power Electron.*, vol. 4, no. 1, pp. 116–125, Mar. 2016.
[34] P. C. Krause, O. Wasynczuk, and S. D. Sudhoff, *Analysis of Electric Machinery and Drive Systems*, 2nd ed. Piscataway, NJ, USA: IEEE Press, 2002.
[35] S. Skogestad and I. Postlethwaite, *Multivariable Feedback Control: Analysis and Design*, vol. 2. New York, NY, USA: Wiley, 2007.
[36] J. Perez, S. Cóbreces, R. Grino, and F. Rodriguez, "$\mathcal{H}_\infty$ current controller for input admittance shaping of VSC-based grid applications," *IEEE Trans. Power Electron.*, vol. 32, no. 4, pp. 3180–3191, Apr. 2017.

Jorge Pérez (S'16–M'17) was born in Madrid, Spain, in 1988. He received the B.Sc., M.Sc., and Ph.D. degrees in industrial electronics from the University of Alcalá (UAH), Alcalá de Henares, Spain, in 2011, 2013, and 2017, respectively.

Until 2017, he was a Researcher for GEISER Group, UAH. He is currently with Gamesa Electric S.A.U., Madrid, Spain. His research interests include automatic control applied to power electronic systems, power quality, and distributed power generation systems.

Santiago Cóbreces (S'03–M'09) was born in Alcalá de Henares, Spain, in 1980. He received the B.Sc. and M.Sc. degrees in telecom engineering, and the Ph.D. degree in electronics engineering from the University of Alcalá (UAH), Alcalá de Henares, Spain, in 2003 and 2009, respectively.

Since 2012, he is an Associate Professor in the Department of Electronics, UAH, where he is a member of the Research Group "Electronics engineering applied to the renewable energies." His current research interests include automatic control and system identification applied to power electronic systems, power quality, and distributed power generation systems.

Robert Griñó (M'99–SM'12) received the M.Sc. degree in electrical engineering, and the Ph.D. degree in automatic control from the Universitat Politècnica de Catalunya (UPC), Barcelona, Spain, in 1989 and 1997, respectively.

From 1990 to 1991, he was a Research Assistant in the Instituto de Cibernética, UPC. From 1992 to 1998, he was an Assistant Professor in the Department of Automatic Control, UPC, where he has been an Associate Professor since 1998. His research interests include digital control, nonlinear control, and control of power electronics converters.

Dr. Griñó is an Affiliate Member of the International Federation of Automatic Control (IFAC) and a Member of the Spanish Society on Automation and Control-IFAC.

Francisco Huerta (S'08–M'11) received the M.Sc. and Ph.D. degrees in electronics engineering from the University of Alcalá (UAH), Alcalá de Henares, Spain, in 2006 and 2011, respectively.

From 2007 to 2012, he was in UAH. From 2013 to 2016, he was a Postdoctoral Researcher in IMDEA Energy. From 2016 to 2017, he worked as a Researcher in UAH. He is currently an Assistant Professor in Carlos III University of Madrid, Madrid, Spain. His research interests include control of power electronics converters, power quality, and distributed power generation systems.

Francisco J. Rodríguez Sánchez (S'99–M'00) received the B.Sc. degree in technical telecommunication engineering from the University of Alcalá (UAH), Alcalá de Henares, Spain, in 1985, the M.Sc. degree in telecommunication from the Technical University of Madrid, Madrid, Spain, in 1990, and the Ph.D. degree in electronics engineering from UAH, in 1997.

He worked in the private electronic industry for two years. Since 1986, he has been a Lecturer in the Department of Electronics, UAH, where he is currently a Professor. He is the author of more than 142 refereed publications in international journals, book chapters, and conference proceedings. He has also directed more than 45 investigation projects funded by public institutions and private industry. His research interests include the areas of control electronics, real-time processing, and embedded systems applied to power electronic systems.